Chemical Science

ROYAL SOCIETY OF CHEMISTRY

EDGE ARTICLE

View Article Online
View Journal | View Issue

Cite this: *Chem. Sci.*, 2021, **12**, 14143

All publication charges for this article have been paid for by the Royal Society of Chemistry

Received 17th April 2021
Accepted 4th October 2021

DOI: 10.1039/d1sc02174e

rsc.li/chemical-science

A combined computational and experimental study of methane activation during oxidative coupling of methane (OCM) by surface metal oxide catalysts†

Daniyal Kiani, Sagar Sourav, Israel E. Wachs * and Jonas Baltrusaitis *

The experimentally validated computational models developed herein, for the first time, show that Mn-promotion does not enhance the activity of the surface Na_2WO_4 catalytic active sites for CH_4 heterolytic dissociation during OCM. Contrary to previous understanding, it is demonstrated that Mn-promotion poisons the surface WO_4 catalytic active sites resulting in surface WO_5 sites with retarded kinetics for C–H scission. On the other hand, dimeric Mn_2O_5 surface sites, identified and studied *via ab initio* molecular dynamics and thermodynamics, were found to be more efficient in activating CH_4 than the poisoned surface WO_5 sites or the original WO_4 sites. However, the surface reaction intermediates formed from CH_4 activation over the Mn_2O_5 surface sites are more stable than those formed over the Na_2WO_4 surface sites. The higher stability of the surface intermediates makes their desorption unfavorable, increasing the likelihood of over-oxidation to CO_x, in agreement with the experimental findings in the literature on Mn-promoted catalysts. Consequently, the Mn-promoter does not appear to have an essential positive role in synergistically tuning the structure of the Na_2WO_4 surface sites towards CH_4 activation but can yield MnO_x surface sites that activate CH_4 faster than Na_2WO_4 surface sites, but unselectively.

1. Introduction

Methane (CH_4) the main component of natural gas, is a sustainable energy vector and an emerging building block for synthesis of chemicals and fuels.[1–5] Direct CH_4 conversion to ethylene (C_2H_4) *via* oxidative coupling of methane (OCM) remains an active research frontier with ongoing studies in both catalysis science and reaction engineering.[6–9] Despite continued interest, the lack of the fundamental understanding of the structure–function relationships in the state-of-the-art OCM catalysts has prohibited industrial-scale application of OCM.[2,10,11] Recent work on selective OCM catalyst development chiefly focuses on the combinatorial screening of multicomponent mixed-phase catalyst systems as well as scrutinizing developed catalyst libraries using data science methods.[7,12–14] The structure–activity relationships of any catalyst, however, are the foundation for rational design and optimization of heterogeneous catalysts.[15–17] Under typical OCM reaction conditions ($CH_4 + O_2$ and high temperatures of up to 850 °C), the catalytic active sites are not mere static geometric forms obtained on calcined supports but undergo dynamic rearrangement dictated by thermodynamics.[18,19] Therefore, well-defined catalysts under reaction conditions should be investigated in order to understand the fundamental OCM catalyst structure–activity relationships.

Dispersed phase catalysts offer key advantages over catalysts containing a mixture of dispersed and crystalline phases,[16,20–23] since dispersed phase catalysts consist of atomically dispersed sites with well-defined molecular and electronic structure that can be tuned *via* the addition of promoters. Such control of the nature and the structure of catalytic active sites remains challenging in the presence of a crystalline phase in supported mixed phase catalysts, which exhibit an ensemble distribution of the catalytic active sites distributed in the various phases, hence complicating the structure–activity analysis. This difference in dispersed *vs.* mixed phase catalysts is illustrated in Fig. 1 using silica (SiO_2) supported metal oxide (MO_x) catalysts, such as those used for OCM, with well-defined active sites found in dispersed phase catalysts allowing systematic analysis for structure–activity relationships, and supported mixed oxide phase catalysts resulting in an variety of various types of sites.

The structure–activity relationships for the state-of-the-art supported Mn–Na_2WO_4/SiO_2 tri-metal oxide OCM catalyst have remained elusive not only due to the demanding reaction conditions, but also due to the mixed-oxide phase nature of this catalyst.[24] While dispersed phase tri-metal oxide catalysts, *i.e.*, containing all three metal oxides (W, Na, Mn), have not been studied to date, the structure–activity relationships of active

Department of Chemical and Biomolecular Engineering, Lehigh University, B336 Iacocca Hall, 111 Research Drive, Bethlehem, PA 18015, USA. E-mail: job314@lehigh.edu; iew0@lehigh.edu

† Electronic supplementary information (ESI) available. See DOI: 10.1039/d1sc02174e

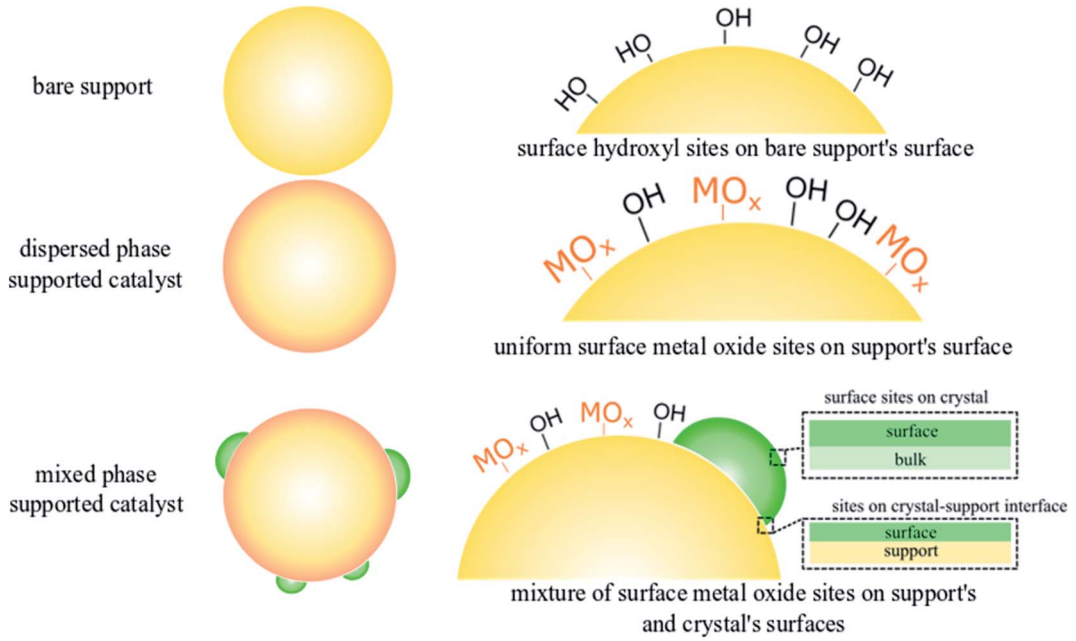

Fig. 1 The nature and type of surface sites on SiO_2 support, dispersed and mixed-phase supported tungsten oxide catalysts used in OCM. The support contains surface hydroxyls (–OH) where the active metal oxides (MO_x such as WO_x, MnO_x) anchor in dispersed phase catalysts. For the supported mixed-oxide phase catalysts, the dispersed phase metal oxide anchors onto the surface –OH sites of the support and the crystalline phase is also present resulting in a wide range of metal oxide sites, along with those present at the interface of the crystal-support.

sites in dispersed phase bi-metal oxide catalysts ($Na–WO_x/SiO_2$, $Mn–WO_x/SiO_2$) for OCM have been recently reported.[22,25] It was shown that the distorted surface WO_4 sites are present at elevated temperatures (673 K) on the amorphous SiO_2 surface in unpromoted, supported WO_x/SiO_2 catalysts.[22] Upon Na-promotion, the extent of distortion of the WO_4 surface site diminishes.[22,25] The dispersed-phase Na-coordinated WO_4 surface sites ($Na–WO_4$) with Na/W molar ratio less than 2 were shown to be significantly more selective to C_2 products than the unpromoted, surface WO_4 sites and the corresponding mixed-oxide phase catalysts containing crystalline phase Na_2WO_4 (Na/W ~ 2).[22,25] Moreover, the promotion with Mn *i.e* $Mn–WO_x/SiO_2$, did not have a significant impact on the molecular structure and OCM C_2 selectivity of the WO_4 surface sites in comparison to unpromoted WO_4 surface sites.[25] Thus, the role of Mn for the OCM catalytic reaction remains unclear.

Older studies of mixed-phase tri-metal oxide catalysts under/near OCM reaction conditions revealed that Mn^{3+} reduces to Mn^{2+} during CH_4 activation, which can then be re-oxidized to Mn^{3+} during the second half of the OCM reaction redox cycle.[26] Based on the proposed $Mn^{3+} \rightarrow Mn^{2+} \rightarrow Mn^{3+}$ redox cycle, multiple reaction models suggesting Mn sites as the catalytic active site during OCM have been put forth in the literature.[26–29] Note that the observed redox cycle, however, was purely based on transitions observed in the crystalline phases of manganese oxide (Mn_2O_3 and Mn_3O_4) and the redox behavior of the dispersed phase manganese oxide surface sites (MnO_x) in the catalyst are still not known. More recently, an *operando* synchrotron μ-XRF/XRD/absorption-computed tomography investigation of the mixed-phase tri-metal oxide catalyst found that during phase transformations occurring in the crystalline manganese oxide phases (Mn_2O_3, Mn_7SiO_{12} and $MnWO_4$), product distribution did not change. Hence, it was concluded that such manganese oxide phases did not have a critical role in the catalytic OCM reaction.[30] It was further concluded that dispersed phase MnO_x surface sites present on the SiO_2 support in the mixed-phase tri-metal oxide catalyst, which bulk X-ray based techniques such as XRD, XAS, XRF cannot effectively monitor, may be involved in the OCM catalytic cycle.[30]

Herein, we provide the first *in silico* framework validated with *in situ* spectroscopy measurements to study the structure–activity relationship of metal oxide sites in model tri-metal oxide OCM catalysts containing Mn, W, Na metal oxides on a SiO_2 support. In particular, the nature and structure of the tri-metal oxide surface sites ($Mn–Na_2WO_4/SiO_2$) was elucidated and contrasted with the bi-metal oxide surface sites (Na_2WO_4) *via ab initio* molecular dynamics (AIMD) and periodic density functional theory (DFT). Na_2WO_4 surface sites are used as the base for this comparison as these surface sites were shown to be the selective active sites for CH_4 activation during OCM.[19,22,25] The DFT predicted molecular and electronic structures of the dispersed phase surface sites in bi- and tri-metal oxide OCM catalyst prior to CH_4 activation were also validated by *in situ* Raman and *in situ* UV-Vis diffused reflectance (UV-VisDR) spectroscopies at dehydrated oxidative conditions (400 °C, 10% O_2/inert), respectively. Intrinsic kinetics of CH_4 dissociation over surface sites in dispersed phase bi-metal oxide and tri-metal oxide case were calculated and contrasted. Results herein provide molecular-level insights on the nature of surface sites, and their activity towards heterolytic CH_4 dissociation during

OCM, providing structure–function relationships for this OCM catalyst.

2. Experimental

(a) Computational modelling

The periodic calculations have been performed with the Vienna *Ab Initio* Simulation package (VASP) using the Perdew and Wang (PW91) generalized gradient approximation exchange–correlation functional. PW91 exchange–correlation functional is used as model used herein are adapted from prior models of supported WO_x catalysts published in the literature.[25,31,32] The valence electrons are treated explicitly and their interactions with the ionic cores are described by the Projector Augmented-Wave method (PAW), which allows using low energy cut off equal to 400 eV for the plane-wave basis. A sampling of the Brillouin zone with $2 \times 2 \times 1$ mesh was applied for all models in this work. The positions of the two top-most layer surface slab atoms, as well as the active (un)coordinated WO_x site, in the supercell, were relaxed until the total energy differences decrease below 10^{-6} eV (forces acting on atoms fall below 0.005 eV $Å^{-1}$). The details of the model of the hydroxylated β-cristobalite slab can be found elsewhere.[25]

Vibrational modes have been calculated for the selected surface species within the harmonic approximation. Only the tungsten active center and its 1st and 2nd neighbors (O–Si and OH groups) were considered in the Hessian matrix. This matrix was computed by the finite difference method followed by a diagonalization procedure. The eigenvalues of the resulting matrix led to frequency values. The assignment of the vibrational modes was done by inspection of the corresponding eigenvectors. Static (NSW = 0, IBRION = −1) self-consistent calculations were performed to compute DOS (ISMEAR = 0, Sigma = 0.02), and the resulting vasprun.xml files were visualized using P4Vasp[33,34] to extract local and total density of states (LDOS, total DOS).

Ab initio molecular dynamics (AIMD) calculations were performed using Anderson thermostat (1700 K, 2 fs steps) to provide sufficient kinetic energy to the simulated catalyst surface for the atoms to rearrange so the global minima for the total energy can be calculated. The antiferromagnetic configuration in dimeric Mn_2O_x cases was consistently lower in energy than ferromagnetic configurations, so all dimeric Mn_2O_x studied here were treated as antiferromagnetic. Typically, ~8000 fs AIMD simulations resulted in 3–4 lowest energy structures, which were then extracted and further optimized by periodic DFT before subsequent calculations were conducted for frequencies, Bader[35] charges and transition states (from nudged elastic band (NEB)[36,37]) on the lowest energy structure amongst the 3–4 selected from AIMD. *Ab initio* thermodynamics (AITD) were calculated according to the framework described in the recent literature.[13,38–40] Specifically, the relative stability of various possible surface Mn_aO_b clusters were computed in reference to the bulk α-Mn_2O_3 phase (unit cell: 32Mn atoms, 48O atoms),[41] which is typically reported to be stable under OCM relevant conditions (T = 1000 K, P_{O_2} = 0.33–0.1).[42] The Mn_2O_3 atom positions and cell parameters were relaxed with high precision and cutoff energy of 520 eV to minimize any Pulay stress. Given the unit cell of α-Mn_2O_3 containing 32Mn and 48O atoms, the general governing stoichiometric equation can be written as (1)

$$(Mn_aO_b \cdot Na_2WO_4)/SiO_2 = \frac{a}{32}Mn_2O_3 + \left[b - \left(48 \times \frac{a}{32}\right)O\right] + Na_2WO_4/SiO_2, \quad (1)$$

with the overall exergonicity or endergonicity of the reaction to form isolated Mn_aO_b clusters, rather than bulk Mn_2O_3, on Na_2WO_4/SiO_2 described *via* (2)

$$\Delta G(T,\ P) = \mu((Mn_aO_b \cdot Na_2WO_4)/SiO_2) - \frac{a}{32}\mu(Mn_2O_3) - \left[b - \left(48 \times \frac{a}{32}\right)\right]\mu(O) - \mu(Na_2WO_4/SiO_2). \quad (2)$$

In this method, the PV contributions of solids were neglected,[13,38–40] and the Gibbs free energies of solids were approximated as their respective electronic energies computed by DFT with thermal corrections in accordance with the methodology described in the literature,[43] as shown in eqn (3)

$$\mu(\text{solid}) = E_{0K}^{DFT}(\text{solid}) + G_{vib}(T). \quad (3)$$

The chemical potential of the gas phase O_2 depends on the temperature (T) and the corresponding partial pressure (P). At arbitrary T and P, μ_{O_2} can then be written as:

$$\mu_{O_2}(T,\ P) = E_{O_2}^{DFT} + E_{O_2}^{ZPE} + \Delta\mu(T,\ P^\circ) + RT\ln(P/P^\circ) \quad (4)$$

here, R is the gas constant, 300 K is the reference T, and 1 atm (101 325 Pa; $P/P^\circ = 1$) is the reference pressure. $\Delta\mu(T, P^\circ)$ were taken from JANAF tables.[44] $E_{O_2}^{DFT}$ was the DFT calculated energy of −9.81 eV and $E_{O_2}^{ZPE}$ value is 0.098 eV.[45] μ_O (*i.e.* $\frac{1}{2}\mu_{O_2}$) values calculated as a function of T and P are tabulated and plotted in Table S1 and Fig. S1,† respectively, and agree with those reported in the literature.[46,47] Thus, Gibbs free energy of formation (G_{form}) for a specific case can be written as eqn (2), where $\mu(Na_2WO_4/SiO_2)$, $\mu(Mn_aO_b + Na_2WO_4/SiO_2)$, and $\mu(Mn_2O_3)$ are chemical potentials of the solid phases calculated according to eqn (3), while μ_O is the oxygen chemical potential calculated according to eqn (4).

For example, using the general eqn (1), the Mn_1O_1–Na_2WO_4/SiO_2 system was calculated as:

$$(Mn_1O_1 \cdot Na_2WO_4)/SiO_2 = \frac{1}{32}Mn_2O_3 + \left[1 - \frac{48}{32}\right]O + Na_2WO_4/SiO_2, \quad (5)$$

with

$$\Delta G(T,P) = \mu(Mn_1O_1 \cdot Na_2WO_4/SiO_2) - \left(\frac{1}{32}\mu(Mn_2O_3) - \frac{1}{2}\mu_O + \mu(Na_2WO_4/SiO_2)\right). \quad (6)$$

Using eqn (1), the comprehensive Mn_aO_b chemical potential landscape was computed for various mono-atomic (Mn, MnO, MnO_2, MnO_3) and di-atomic (Mn_2O, Mn_2O_2, Mn_2O_3, Mn_2O_4,

Mn_2O_5 compositions to compare their respective thermodynamic stability given OCM relevant conditions of 1000 K and P_{O_2}/P° of 0.1–0.33. A higher degree of oligomerization for surface Mn_aO_b compositions was not considered due to the complexity of the possible structures in tri- and tetra-atomic cases such as straight 2D-chain *vs.* 3D-clusters.

Lastly, intrinsic rate constant (k_d°) of C–H dissociation in CH_4 was calculated using the DFT-computed E_0 values of transition states identified *via* NEB method, according to equation:

$$k_d^\circ(s^{-1}) = \frac{K_B T}{h} e^{\frac{-E_a}{RT}}, \quad (7)$$

where k_B is the Boltzmann constant (J K^{-1}), h is the Planck's constant (J s), T is the reaction temperature (K), R is the gas constant (J K^{-1} mol^{-1}), and E_a is the energy difference with E_0 values of initial and transition state structures in J mol^{-1}.

(b) Non-stoichiometric catalyst synthesis

The SiO_2 support (Cabot CAB-O-SIL® EH5 with a surface area of ~332 m^2 g^{-1}) was first treated with water, then allowed to dry overnight at room temperature before final calcination at 500 °C for 4 hours under flowing air. This treatment increases the density and surface hydroxyls of the SiO_2 support. The dried SiO_2 obtained after calcination was then crushed into a fine powder. The resulting pore volume of the SiO_2 powder was determined to be ~0.8 mL g^{-1} and was utilized for all catalyst preparation steps *via* incipient-wetness impregnation (IWI) of the metal oxide aqueous solutions unless mentioned otherwise. A NaOH aqueous solution corresponding to the pore-volume equivalent of ~0.8 mL g^{-1} was impregnated onto the SiO_2 support and the sample was initially dried overnight, then at 120 °C in an oven under flowing air for 2 hours, and finally calcined at 700 °C under airflow for 2 hours. The resultant supported Na/SiO_2 sample, with pore volume equivalent of ~0.7 mL g^{-1}, was subsequently impregnated with the desired aqueous concentration of W in the form of AMT ($(NH_4)_xW_{12}O_{28}$; Alfa Aesar, #44792) and Mn in the form of $Mn(NO_3)_2$ (Alfa Aesar, #10806-09). The resultant solid was dried overnight, then at 120 °C for 2 hours in airflow and finally calcined at 500 °C for 4 hours under flowing air. The final catalysts were denoted as 8% $W/0.4\%Na/SiO_2$ (Na/W = 0.4)[22] in the bi-metal oxide case and $0.5\%Mn–8\%W/0.4\%Na/SiO_2$ (Na/W = 0.4, Mn/W = 0.2) in the tri-metal oxide case. Samples calcined at 500 °C calcination did not undergo sintering typical of higher temperature calcination, enabling easier characterization of the surface metal oxide sites, which becomes challenging in low surface area sintered materials.

(c) *In situ* Raman spectroscopy

The *in situ* Raman spectra of the Na coordinated WO_x/SiO_2 supported catalysts were obtained with Horiba–Jobin Yvon LabRam HR instrument equipped with three laser excitations (532, 442, and 325 nm) and liquid N_2-cooled CCD detector (Horiba–Jobin Yvon CCD-3000 V). The 442 nm laser was chosen for spectral accumulation since it minimizes sample fluorescence from the SiO_2 supported catalysts. The wavenumber calibration was checked using a standard silicon wafer with a Raman vibration at 520.7 cm^{-1}. A confocal microscope with a 50× objective (Olympus BX-30-LWD) was utilized for focusing the laser on the catalysts. Typically, the spectra were collected for 60 s per scan for a total of three scans with a 1000 μm hole with a spectral resolution of ~1 cm^{-1}. Approximately 15–20 mg of each catalyst in powder form (100–150 μm size range) was loaded into an environmental cell (Linkam CCR-1000) with a quartz window with O-ring seals, which was kept cool by circulating cooling water. The *in situ* Raman spectra of the catalysts were collected at 400 °C after dehydration in 10% O_2/Ar (~30 cc min^{-1}) for 60 min to elucidate the initial molecular structure of the representative bi- and tri-metal oxide surface sites to validate the DFT-optimized structures before reaction with CH_4.

(d) *In situ* UV-Vis DR spectroscopy

The *in situ* UV-Vis spectra of the catalysts were obtained using a Varian Cary 5E UV-Vis-NIR spectrophotometer with a Harrick Praying Mantis accessory. Approximately 15–20 mg of each catalyst in powder form was loaded into an *in situ* Harrick HVCDR2 environmental cell. The UV-Vis spectra of the catalyst samples were collected at 400 °C in the 200–800 nm wavelength range after dehydration (10% O_2/Ar, ~30 cc min^{-1}) for 60 min, using a scan rate of 15 nm min^{-1} and a signal averaging time of 0.6 s. MgO was used as a standard for obtaining the background absorbance and was subtracted from the sample absorbance. Kubelka–Munk function $F(R_\infty)$ was calculated from the background-subtracted absorbance data of the UV-Vis spectrum of each sample. The edge energy (E_g), or bandgap, was determined by finding the intercept of the straight line for the low-energy rise of a plot of $[F(R_\infty)h\nu]^2$ *versus* $h\nu$, where $h\nu$ is the incident photon energy. The *in situ* UV-Vis spectra of the catalysts at 400 °C after dehydration in 10% O_2/Ar were used to elucidate the initial electronic structure of the representative bi- and tri-metal oxide surface sites to validate the DFT-optimized structures before reaction with CH_4.

3. Results and discussion

(a) Thermodynamic stability of Mn_aO_b–Na_2WO_4/SiO_2 catalysts under OCM relevant conditions

The Gibbs free energies of formation ($\Delta G(T, P)$ further referred to as ΔG_{form}) of Mn_aO_b surface sites in Na_2WO_4/SiO_2 catalysts were computed as a function of oxygen partial pressure according to eqn (2) with respect to the bulk Mn_2O_3 phase. In an oxygen containing reaction mixture, the surface Mn_aO_b sites are expected to be oxidized depending on the partial pressure of the oxygen. Therefore, as a starting point, ΔG_{form} was computed for four possible mono-atomic Mn_1O_b cases Mn, MnO, MnO_2, and MnO_3, where b is 0, 1, 2 and 3, respectively. As shown in the heat maps in Fig. 2a–d, the redder tones signify positive values of ΔG_{form} and bluer tones signify negative ΔG_{form}. Positive ΔG_{form} imply that formation of that cluster is endergonic with respect to bulk Mn_2O_3, while negative values imply that the formation of that cluster is exergonic with respect to bulk Mn_2O_3. Fig. 2a–

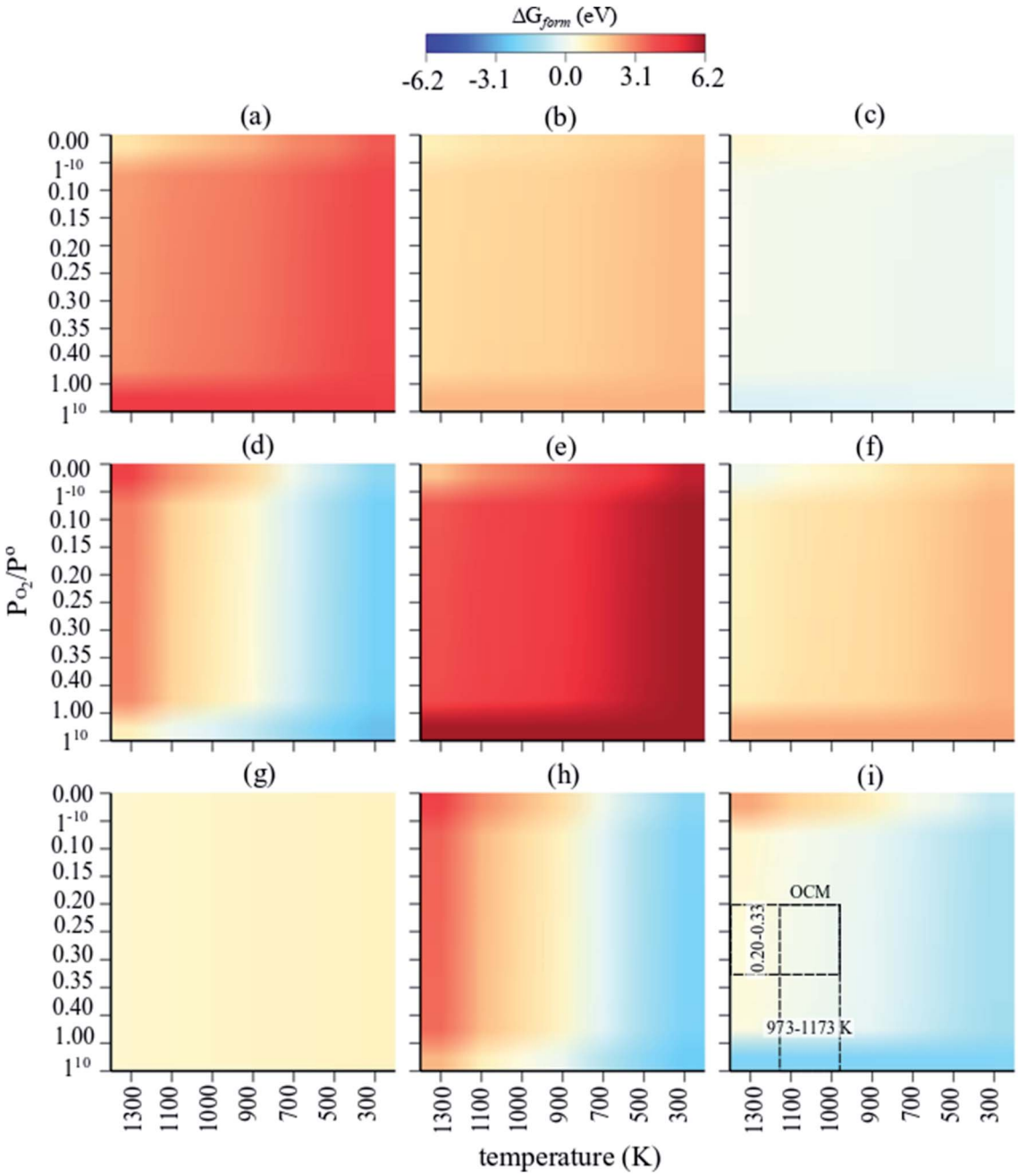

Fig. 2 Individual heat maps of computed Gibbs free energy of formation for (Mn_aO_b–Na_2WO_4)/SiO_2 as a function of T (300–1300 K) and P_{O2}/P = 0–1 (ref. 10) for (a) Mn, (b) MnO, (c) MnO_2, (d) MnO_3, (e) Mn_2O, (f) Mn_2O_2, (g) Mn_2O_3, (h) Mn_2O_4, (i) Mn_2O_5. The dashed rectangle in (i) signifies the OCM relevant conditions.

d show that the formation of isolated Mn, MnO, MnO_3 surface sites are clearly endergonic in comparison to bulk Mn_2O_3 under OCM conditions (~973–1173 K, P_{O_2}/P = 0.20–0.33). However, the isolated MnO_2 formation is barely endergonic relative to bulk Mn_2O_3 under OCM conditions and in fact becomes exergonic at high P_{O_2} and low temperatures. Likewise, five stoichiometries possible considered for the di-atomic Mn_2O_b are Mn_2O, Mn_2O_2, Mn_2O_3, Mn_2O_4, and Mn_2O_5 where b is 1, 2, 3, 4, and 5 respectively. The computed ΔG_{form} for each case are shown as heat maps in Fig. 2e–i. At OCM conditions, besides Mn_2O_5, the formation of di-atomic sites (Mn_2O, Mn_2O_2, Mn_2O_3, Mn_2O_4) is endergonic in reference to the bulk Mn_2O_3 and thus unfavorable. Therefore, under OCM conditions, formation of Mn_2O_5 sites yielding Mn_2O_5–Na_2WO_4/SiO_2 catalyst the most thermodynamically favorable from an AITD standpoint.

In a comparison shown in Fig. 3, the entire catalyst structure space of Mn_aO_b–Na_2WO_4/SiO_2 was compared to ascertain the most thermodynamically stable stoichiometry of surface Mn_aO_b sites in Mn_aO_b–Na_2WO_4/SiO_2 catalysts under OCM relevant P_{O_2}/P° of 0.2–0.33, and temperature of 1000 K. Under these

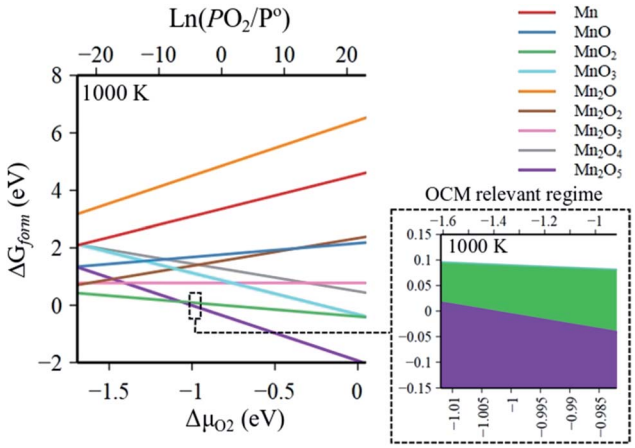

Fig. 3 Global comparison of Gibbs free energy of formation of $(Mn_aO_b–Na_2WO_4)/SiO_2$ at OCM relevant conditions (P_{O_2}/P° = 0.20–0.33 at 1000 K) identifying $Mn_2O_5–Na_2WO_4/SiO_2$ as the most thermodynamically stable structure under these conditions.

conditions, the formation of Mn_2O_5 dimeric sites is evidently thermodynamically favorable (*i.e.* most exergonic) with reference to bulk Mn_2O_3, especially towards P_{O_2}/P° values ~0.30–0.33 that represent the OCM reaction stoichiometry *i.e.* $CH_4 : O_2 = 2 : 1$. For instance, as the P_{O_2}/P° values increase from 0.25 to 0.35, the ΔG_{form} of Mn_2O_5 sites decreases from −0.002 eV (−0.20 kJ mol^{-1}) to −0.031 eV (−3.00 kJ mol^{-1}). Note that since the Gibbs energy difference is so small between MnO_2 and Mn_2O_5, a minor presence of MnO_2 sites cannot be precluded under OCM conditions in the catalyst. However, for simplicity, the $Mn_2O_5–Na_2WO_4/SiO_2$ catalyst was chosen for further study presented in the next sections. Specifically, the molecular and electronic structure of the surface sites in $Mn_2O_5–Na_2WO_4/SiO_2$ catalyst are calculated and compared against the base case of unpromoted Na_2WO_4/SiO_2 to ascertain the effect of Mn promotion. The base case *i.e.* Na_2WO_4/SiO_2 contains Na-coordinated WO_4 surface sites that have been shown to be the selective active sites for OCM in such bi-metal oxide catalysts.[22,25] Moreover, the molecular and electronic structures of DFT-optimized structures are also validated against experimental *in situ* characterization data to ensure agreement. Lastly, CH_4 activation pathways and intrinsic kinetics are also compared in each case to elucidate the role of surface Mn sites in OCM.

(b) Molecular structure of surface sites in Na_2WO_4/SiO_2 and $Mn_2O_5–Na_2WO_4/SiO_2$

The DFT-optimized molecular structure of surface sites in Na_2WO_4/SiO_2 and $Mn_2O_5–Na_2WO_4/SiO_2$ are shown in Fig. 4a. In the case of Na_2WO_4/SiO_2, bi-grafted, dioxo WO_4 surface site is present in a distorted T_d geometry, in agreement with experimental and computational work previously reported in the literature.[22,25] On the other hand, the molecular structure of $Mn_2O_5–Na_2WO_4/SiO_2$ contains surface WO_x site that changes dramatically in terms of its molecular structure due to interaction with the surface Mn_2O_5 dimer. In this case, the bi-grafted, di-oxo WO_x is coordinated to the adjacent Mn_2O_5 site *via* a single W–O–Mn bond, and so can be regarded as WO_5. The Mn_2O_5 is present as a dimer bridged *via* a single Mn–O–Mn bond with both MnO_4 units present as distorted pseudo tetrahedral (T_d).

Fundamental frequencies for each case were computed and contrasted with experimental *in situ* Raman spectra of representative dehydrated catalysts to validate the computational model against experimentally observed structures, as shown in Fig. 4b and c. In each case, the computed fundamental modes

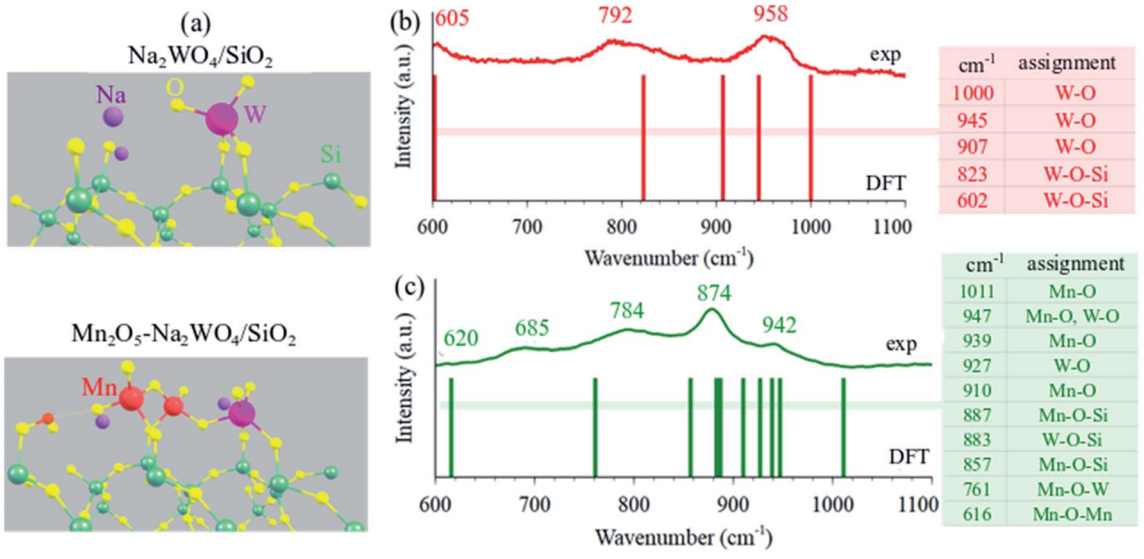

Fig. 4 (a) Periodic DFT optimized structures minimum energy structures for Na_2WO_4/SiO_2 and $Mn_2O_5–Na_2WO_4/SiO_2$ catalysts. Comparison of experimental *in situ* dehydrated Raman (400 °C, 10% O_2/N_2, 532 nm) and DFT calculated frequencies from 600–1200 cm^{-1} for (b) Na_2WO_4/SiO_2 and (c) $Mn_2O_5–Na_2WO_4/SiO_2$ OCM catalysts. The vibrations from SiO_2 support are not shown/labelled herein for clarity. The presence of poorly crystalline Mn–WO_3 and $MnWO_4$ nanoparticles is inferred as well from the experimental *in situ* Raman spectrum in (c).

are assigned in the color-coded tables in Fig. 4b and c and the solid bars are the DFT-calculated frequencies. In both cases, general agreement is observed between computed frequencies and experimentally measured Raman bands, validating the DFT-optimized structural models. From this comparison, it is inferred that W=O bonds are the shortest, given they vibrate in the 945–1000 cm^{-1} range. Likewise, support-grafting bonds like W–O–Si and Mn–O–Si are significantly longer, given they vibrate in the 800–900 cm^{-1} range. Lastly, bridging bonds like Mn–O–Mn and Mn–O–W are the longest (weakest), since they vibrate at 616 and 761 cm^{-1}, respectively. It should be noted that we infer a small presence of poorly crystalline nanoclusters/nanoparticles of $MnWO_4$ and Mn-contaminated WO_3 in the experimental Raman spectrum of the tri-metal oxide catalyst shown in Fig. 4c, which exhibit Raman bands in the same region as dispersed phase sites. However, since *operando*/*in situ* characterization studies in the literature suggest that crystalline $MnWO_4$ is not critical to OCM,[29,30] and because the nature (size, shape, surface structure, defect density) of these nanoparticles is not known presently, the nanoparticles have been excluded from this computational model and only the dispersed phase surface sites were studied for structure–function relationships towards CH_4 activation. Interested readers are directed to a recent, fully experimental study, where further detailed experimental characterization including UV-VisDRS, Raman at 400 °C, Raman during OCM at 900 °C, TPSR, *etc.* of several model OCM catalysts including the two catalysts compared in Fig. 4b and c can be found.[48]

(c) Electronic structure of surface sites in Na_2WO_4/SiO_2 and Mn_2O_5–Na_2WO_4/SiO_2

Next, the electronic structure of the DFT-optimized models is studied. The calculated Bader charges as well as the bond lengths are shown in Fig. 5a and b for Na_2WO_4/SiO_2 and Mn_2O_5–Na_2WO_4/SiO_2 cases, respectively. In both cases, the W centers have an identical Bader charge of +2.51, which corresponds to an oxidation state of +6 according to the calibration curves shown in Fig. S2,† generated according to literature reported methodology.[49] On the other hand, the calculated Bader charges for the two Mn atoms in Mn_2O_5–Na_2WO_4/SiO_2 catalyst were +1.66 and +1.63, respectively, corresponding to an oxidation state of ~+3 (Fig. S2†), which agrees well with the literature reported Mn oxidation state of +3 under oxidative conditions (*i.e.* no CH_4 at elevated temperatures).[26] Experimental *in situ* UV-Vis DRS was conducted on two representative samples, namely bi-metal oxide Na–WO_x/SiO_2 with Na/W = 0.4, and tri-metal oxide Mn–Na–WO_x/SiO_2 with Na/W = 0.4, Mn/W = 0.5 as shown in Fig. 5d. In both cases, ligand to metal charge transfer

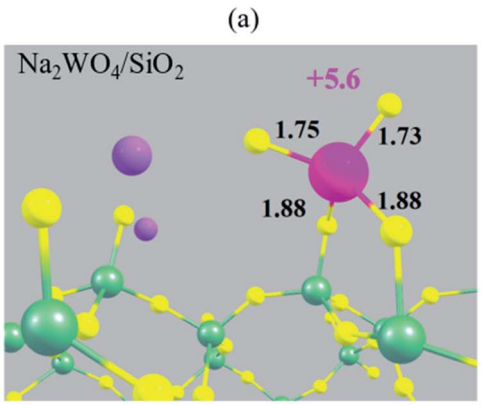

(c)

Description	Na_2WO_4/SiO_2	Mn_2O_5-Na_2WO_4/SiO_2
Na	0.89	0.88
Na	0.84	0.86
W	2.51	2.51
W=O	-0.77	-0.77
W=O	-0.86	-0.86
W-O-Si	-1.25	-1.45
W-O-Si	-1.25	-1.29
Mn	N/A	1.63
Mn	N/A	1.66
Mn-O	N/A	-0.54
Mn-O	N/A	-0.81
Mn=O	N/A	-0.68
W-O-Mn	N/A	-0.91
Mn-O-Mn	N/A	-0.77
Mn-O-Si	N/A	-1.23
Mn-O-Si	N/A	-1.23

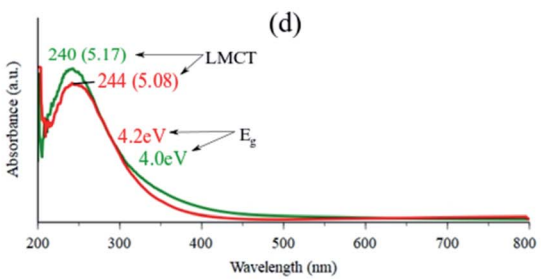

Fig. 5 Structural visualization of (a) Na_2WO_4/SiO_2 and (b) Mn_2O_5–Na_2WO_4/SiO_2 with calculated oxidation states mentioned next to the transition metal atoms in corresponding colors (Mn: red, W: pink). Oxidation states were calculated using a calibrated-fit for Bader charges, shown in Fig. S2 in the ESI section.† Calculated Bader charges for the surface sites in each case are summarized in table (c). (d) *In situ* dehydrated UV-Vis DRS of Na–WO_x/SiO_2(red) and Mn–Na–WO_x/SiO_2(green) catalysts, with E_g values and LMCT positions marked.

energies (~240 nm or 5.1 eV) indicate that W centers were indeed fully oxidized, *i.e.* +6, in agreement with the DFT results.[22,50,51] The edge energy (E_g), indicative of the degree of polymerization of surface sites was ~4.2 eV for Na–WO_x/SiO_2 catalyst, but decreased to 4.0 eV upon Mn-promotion of Na–WO_x sites, suggesting Mn-promotion increases polymerization in surface sites. The oxidation state of Mn atoms, on the other hand, cannot be determined from UV-vis DRS as UV-Vis DRS due to the low concentration of Mn in the Mn–Na–WO_x/SiO_2 representative sample and the lower extinction coefficient of MnO_x *vs.* WO_x, the LMCT and d–d bands from Mn centers are masked by the absorbance of W sites.

The E_g value after Mn-promotion of Na–WO_x sites is lower than the E_g value in the Na–WO_x case (Fig. 5d), which can be further understood *via* density of states (DOS) analysis of DFT-optimized structures. Total DOS plots are shown in Fig. 6a and b for Na_2WO_4/SiO_2 and Mn_2O_5–Na_2WO_4/SiO_2, respectively. For the Na_2WO_4/SiO_2 case, the valence band is primarily composed of occupied O 2p and W 5d states, while the conductance band of empty W 5d states. The energy gap between the top of the valence edge and the bottom of the conduction edge is ~1.7 eV. However, in the Mn_2O_5–Na_2WO_4/SiO_2 case, the valence and conductance bands are primarily composed of Mn 3d states, with some contribution from occupied O 2p states in the valence band. In this case, the lowest part of the conductance band lowers due to low-lying unoccupied Mn 3d states, reducing the bandgap to ~0 eV. The DOS analysis shows that Mn-addition fundamentally changes the electronic structure of the surface sites by introducing low-lying vacant Mn 3d states above the Fermi level, which will have strong implications for the catalytic CH_4 activation. Elsewhere, it has been found that low-lying empty d states in a transition metal like Pt can act an acceptor for σ-donation from the C–H bond of CH_4 and lead to facile C–H scission.[52] Thus, it suffices to conclude at this point that experimental *in situ* UV-Vis DRS and computational DOS analysis are in qualitative agreement evidencing that Mn-promotion of Na_2WO_4 surface sites will lower the E_g values due to the introduction of low-lying empty Mn 3d states above the Fermi level, that Mn is present in its +3 oxidation state, and that W is present in its fully oxidized +6 state.

(d) Reaction kinetics of CH_4 dissociation over Mn_2O_5–Na_2WO_4/SiO_2 *vs.* Na_2WO_4/SiO_2

AITD analysis identified Mn_2O_5–Na_2WO_4 as the most stable species under OCM relevant temperature and oxygen partial pressure. Therefore, the intrinsic activity of Na_2WO_4/SiO_2 *vs.* Mn_2O_5–Na_2WO_4/SiO_2 surface sites for CH_4 dissociation were studied, where the C–H bond dissociation is the most kinetically relevant elementary step in the OCM mechanism.[19,53] To

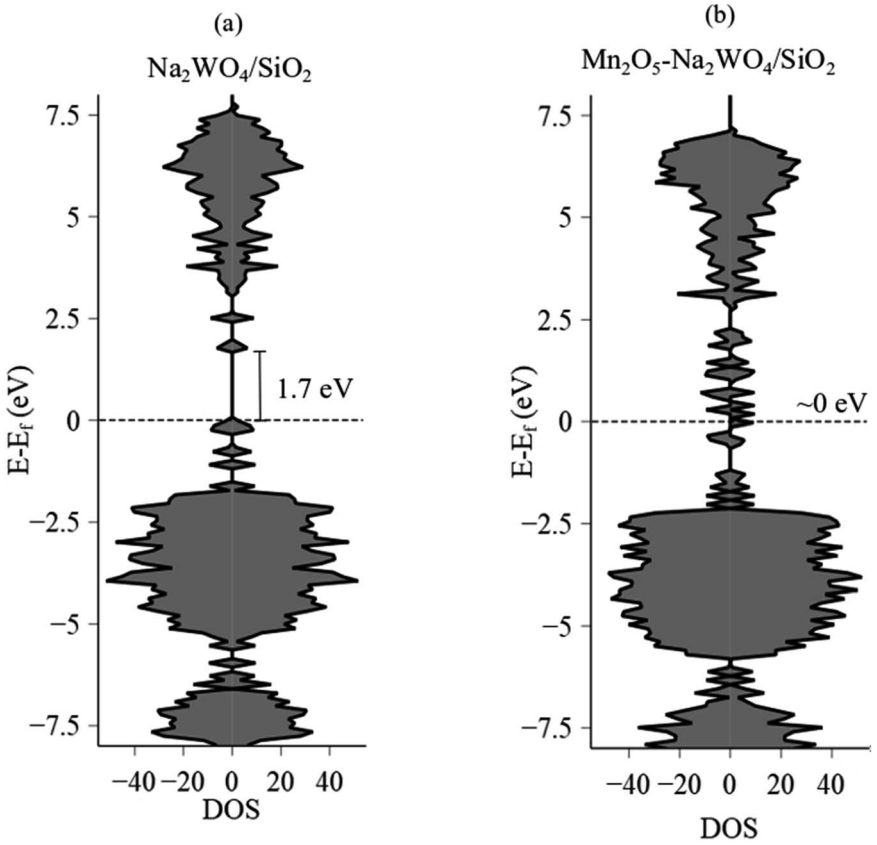

Fig. 6 Total electronic density of states (total DOS) and calculated band gap values (eV) for (a) Na_2WO_4/SiO_2 and (b) Mn_2O_5–Na_2WO_4/SiO_2. E_F values for Na_2WO_4/SiO_2 and Mn_2O_5–Na_2WO_4/SiO_2 were −3.08 eV and −2.75 eV, respectively. The positive *x*-axis values correspond to spin-up, while the negative values correspond to spin-down states.

enhance readability and comprehension, the various possible reaction pathways for heterolytic C–H scission of CH_4 are grouped based on the type of surface intermediate formed in the forward step. Specifically,

$$CH_4 + MO_x \rightarrow M\text{–}O\text{–}CH_3\ (\text{methoxy}) + M\text{–}OH\ (\text{hydroxy}) \quad (8)$$

$$CH_4 + MO_x \rightarrow M\text{–}O\text{–}CH_3 + M\text{–}H\ (\text{hydride}) \quad (9)$$

$$CH_4 + MO_x \rightarrow M\text{–}CH_3\ (\text{methyl}) + M\text{–}OH \quad (10)$$

where MO_x represents a reactive metal oxide surface site (Mn_2O_5 or WO_4). In each case, the surface intermediate pair formed from CH_4 dissociation is unique, *i.e.* methoxy–hydroxy (OCH_3, OH) in the red pathway, methoxy–hydride (OCH_3, H) in the blue pathway and methyl–hydroxy (CH_3, OH) in the green pathway, as shown in Fig. 7 and 9.

CH_4 dissociation over Na_2WO_4 surface sites was studied as a function of the possible pathways listed above, and as a function of various active oxygen atoms. The results are summarized in Fig. 7a–c, highlighting the activation barriers associated with various possible pathways over the Na_2WO_4/SiO_2 catalyst. According to the computed energy barriers summarized in Fig. 7a, the highest energy barrier was for the pathway yielding OCH_3, OH surface intermediates (3.4 eV), indicating that CH_4 dissociation turnover frequency for this pathway will be lower than other pathways with smaller transition state barriers. The two pathways with OCH_3, H intermediates formation differ in terms of the oxygen atom of the WO_4 where C–H scission occurs, and consequently have slightly varying TS barriers (1.6, 1.9 eV). Lastly, the pathway yielding CH_3, OH surface intermediates exhibited the lowest energy barrier of 1.1 eV, suggesting that this is the dominant reaction pathway for CH_4 dissociation over Na-coordinated WO_4 surface sites in the Na_2WO_4/SiO_2 catalysts. The resulting intrinsic rate constants, calculated according to eqn (7) are plotted in Fig. 7b, suggesting that the intrinsic rate constant for the CH_3, OH pathway is 2–3 orders of magnitude higher than other pathways making this the dominant pathway. Lastly, the initial, transition state (TS) and final structures for CH_4 activation over Na_2WO_4 surface sites *via* the dominant reaction pathway are shown in Fig. 7c, showing the formation of W–CH_3 and W–O–H intermediates. Importantly, these results show that Na_2WO_4 surface sites can effectively dissociate CH_4 in the absence of Mn-promoter in agreement with a recently published report,[22] as opposed to Lunsford[19] reaction model where Na–O–Mn sites are assumed to be the critical active sites for CH_4 dissociation.

Local DOS (LDOS) analysis was conducted to elucidate the changes in electronic structure of initial *versus* the TS structure during CH_4 dissociation over the Na_2WO_4 surface sites. LDOS for W 5d states and O 2p states of the initial Na_2WO_4 structure are shown in Fig. 8a. The valence band (below the Fermi level, E_F) is comprised largely of occupied 2p states from the double-bonded oxygen *i.e.* W=O, while the conductance band is comprised largely of unoccupied W 5d states with a minor contribution from unoccupied O 2p states of W=O. Upon CH_4 dissociation, the lowest part of the conductance band lowers in energy as the unoccupied O 2p states get filled. Moreover, significant overlap of occupied states is observed for W 5d and C 2p states near the top of the valence edge at *ca.* −1.7 eV, signifying W–C bond formation as in the W–CH_3 surface intermediate. Lastly, occupied H 1s states and occupied O 2p

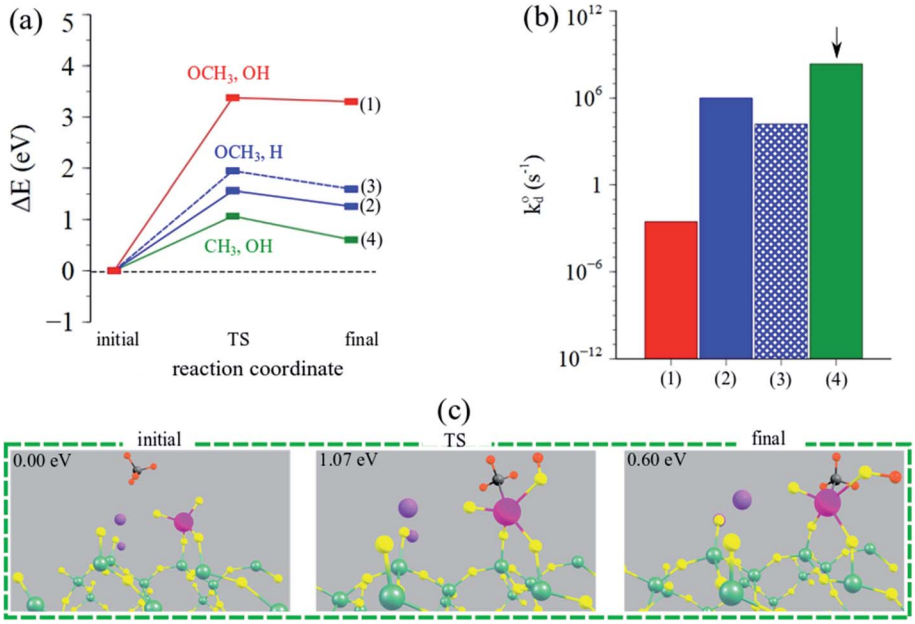

Fig. 7 (a) Reaction coordinate *vs.* ΔE_{DFT} (eV) and (b) calculated intrinsic rate constants (log-scale) for CH_4 dissociation for the three possible pathways over the Na_2WO_4/SiO_2 catalyst. Arrow indicates the dominant (fastest) pathway. (c) Structural depictions of the initial, TS and final states during CH_4 dissociation over Na_2WO_4/SiO_2 catalysts yielding methyl-hydroxy (CH_3, OH) intermediates. Pictorial summary for other pathways can be found in Table S3.†

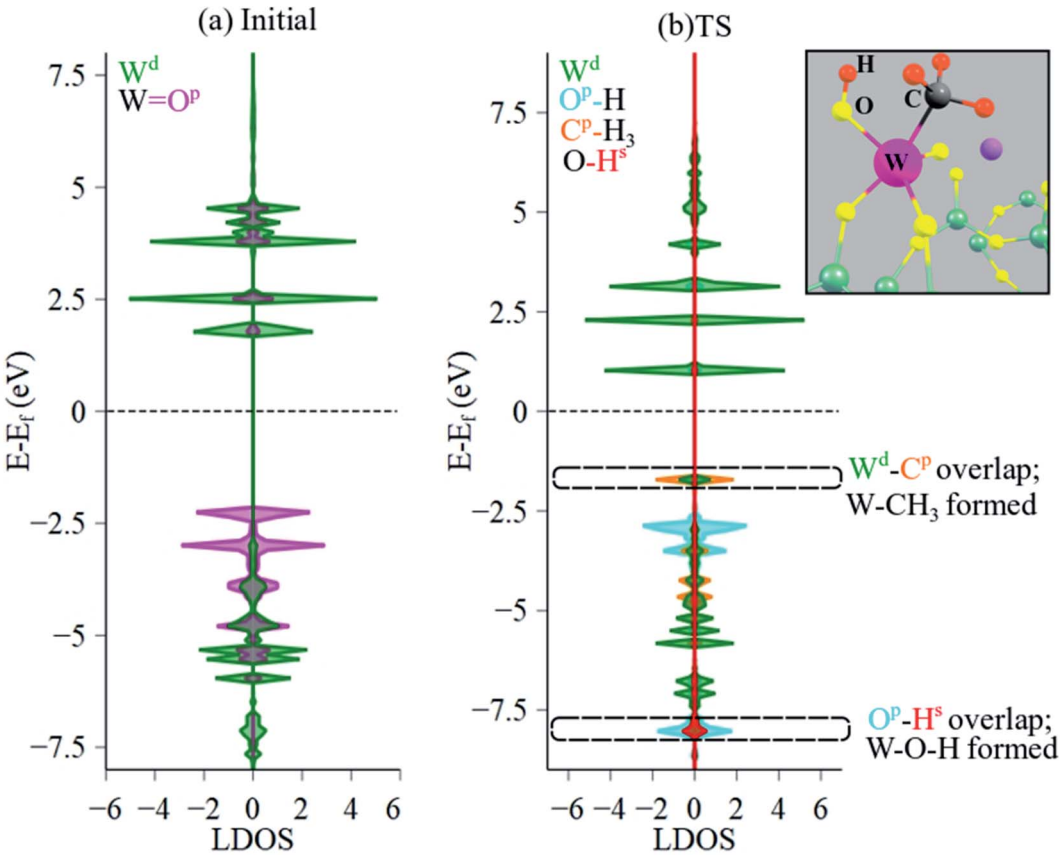

Fig. 8 LDOS analysis of (a) initial and (b) TS structures evidencing W–CH_3 and W–O–H formation, suggesting that CH_4 dissociation is mediated by a TS where a methyl is coordinated to the W center, while H is abstracted by W=O to form W–O–H. The inset shows the zoomed-in structure of the Na_2WO_4 surface site with the pertinent atoms labeled. E_F for the initial structure was −3.08 eV and for the TS was −2.90 eV. Colored atoms correspond to the corresponding color in DOS plots.

states also overlap in the lower part of the valence edge, confirming O–H bond formation *i.e.* W–O–H intermediate. The Bader charge for W barely decreases; it changes from +2.51 in initial structure to +2.48 in the TS structure, indicating minimal reduction of the W center. The partial reduction of W center instead of a full reduction to +5 or to +4 might be the reason that reduced W centers could not be observed during OCM in SQUID-EPR experimentally.[26] Interestingly, a similar CH_4 dissociation pathway yielding CH_3, OH surface intermediates was also proposed for La_2O_3-based catalysts, where La–CH_3 and La–O–H intermediates formed upon heterolytic dissociation of CH_4.[54] Likewise, CH_4 dissociation over Al_2O_3 was also shown to proceed *via* Al–CH_3 and Al–O–H formation.[55]

Next, intrinsic kinetics of CH_4 dissociation over Mn_2O_5–Na_2WO_4/SiO_2 catalyst were studied to ascertain if CH_4 still dissociated over the WO_x like it did in the case of Na_2WO_4/SiO_2 catalyst. Once again, the color-coded pathways signify the unique surface intermediates produced. In this case however, CH_4 dissociation was studied as a function of the moiety since three distinct moieties are present in the surface site *i.e.* WO_5 moiety, W–O–Mn moiety, and Mn_2O_5 moiety. The motivation behind studying CH_4 dissociation as a function of moieties is and to ascertain the affect of Mn_2O_5 promotion on the reaction pathway and intrinsic kinetics. If, CH_4 dissociates preferentially over the Mn_2O_5 moiety, it would indicate that the effect of Mn-promotion in OCM catalysts is not to tune the WO_x surface site but in fact to generate a second active site altogether. On the other hand, if it still activates over WO_5 moiety, the role of Mn_2O_5 would be inferred as a structural/chemical promoter.

As shown in Fig. 9a, CH_4 dissociation becomes energetically unfavorable over the WO_5 moiety *i.e.* 2–4 eV TS barriers, in stark contrast to facile CH_4 dissociation observed over WO_4 site in Na_2WO_4/SiO_2 without Mn_2O_5 promotion (1.1 eV). The higher TS barriers in the case of WO_5 moiety in Mn_2O_5–Na_2WO_4/SiO_2 catalyst in comparison to the pseudo-T_d WO_4 moiety in Na_2WO_4/SiO_2 catalyst are likely due to the loss of T_d geometry of the WO_x center upon Mn_2O_5 promotion, where the T_d WO_4 serves as a reaction site. The T_d geometry of the WO_4 is often regarded as a critical requirement of the selective active site in OCM in various experimental studies,[19,22,25,56–60] and that notion finds support from the DFT results herein.

On the other hand, CH_4 can also dissociate over the W–O–Mn and Mn_2O_5 moieties *via* various pathways with TS barriers in the 1–5 eV range, shown in Fig. 9b and c. Overall, however, the lowest barrier pathway was the one yielding methoxy–hydroxy (OCH_3, OH) intermediates, over the Mn_2O_5 moiety, with a TS barrier of 0.72 eV, which is 0.3 eV lower than the lowest TS barrier pathway for CH_4 activation over Na_2WO_4/SiO_2

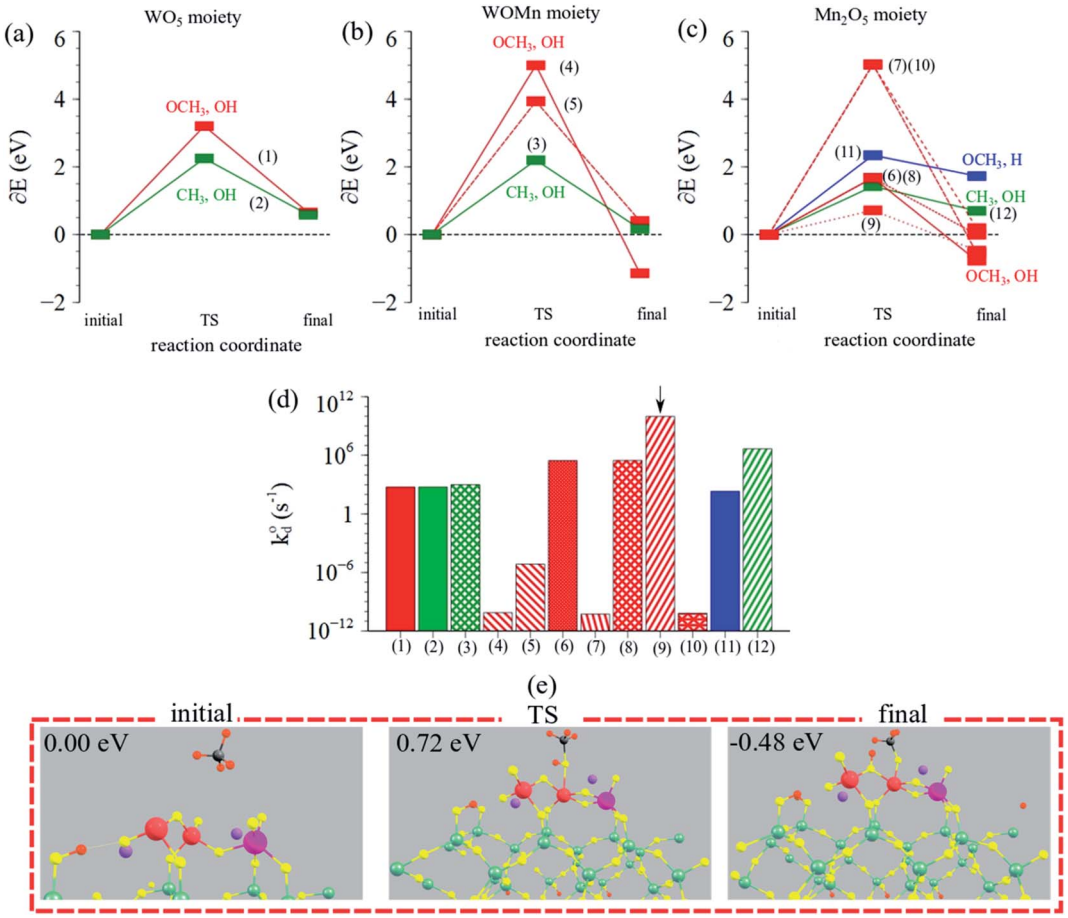

Fig. 9 Reaction coordinate *vs.* ΔE_{DFT} (eV) over (a) WO_5 moiety, (b) W–O–Mn moiety, (c) Mn_2O_5 moiety in Mn_2O_5–Na_2WO_4/SiO_2 catalyst. (d) Calculated intrinsic rate constants (log-scale) for CH_4 dissociation for the possible pathways in Mn_2O_5–Na_2WO_4/SiO_2 catalyst. Arrow indicates the dominant (lowest barrier) pathway. All numbered pathways 1–9 are described in ESI Table S4.† (e) Visualization of the dominant (lowest barrier) pathway for CH_4 dissociation over the Mn_2O_5–Na_2WO_4/SiO_2 catalyst, yielding methoxy–hydroxy (OCH_3, OH) surface intermediates.

in the absence of Mn-promoter. Fig. 9d compares the calculated intrinsic rate constants for CH_4 dissociation across all moieties *via* various pathways studied, showing that the lowest TS barrier pathway indeed exhibits a rate constant orders of magnitude higher than other cases and hence is the dominant pathway. Lastly, initial, TS, and final structures for the dominant reaction pathway in this case are summarized in Fig. 9e, evidencing the involvement of Mn–O and Mn–O–Mn bonds in CH_4 dissociation to yield Mn–O–CH_3 and $(Mn)_2$–O–H surface intermediates.

To ascertain the electronic structural dynamics of the surface sites during CH_4 dissociation, LDOS analysis (Mn 3d, O 2p, C 2p, H 1s states) was conducted for the initial and TS structures of Mn_2O_5–Na_2WO_4/SiO_2, shown in Fig. 10a and b, respectively. Initially, the valence edge is comprised of a mixture of occupied Mn 3d states and O 2p states from Mn–O–Mn and Mn–O bonds. The conductance edge is primarily made up of unoccupied Mn 3d states with some contribution from empty O 2p states. Upon CH_4 dissociation and TS formation, the LDOS changes drastically. The upper part of the valence band lowers in energy, and occupied, spin-up Mn 3d states appear at −2.0 eV, which were not present in the initial structure. Moreover, overlapping O 2p and C 2p states as well as the O 2p and H 1s states confirm formation of Mn–O–CH_3 and $(Mn)_2$–O–H intermediates. In this case, the occupied C 2p states overlap with occupied O 2p states of Mn–O towards the bottom of the valence edge (−7.0 eV). Lastly, Mn Bader charge decreases from +1.63 to +1.55 from initial to TS structure, indicating reduction of the Mn centers from ∼+3 to ∼+2 in agreement with experimental literature.[26,61]

(e) C–H bond activation over surface metal oxide sites

The results presented so far point out that heterolytic dissociation of CH_4 can occur over surface sites, either WO_4 or Mn_2O_5, *via* the Mars–van Krevelen (MvK) mechanism (*i.e.*, involvement of lattice oxygen instead of adsorbed O_2, as inferred from general agreement between TS barriers estimated herein and apparent activation barriers reported in the broader OCM literature in the 100–150 kJ mol^{-1} range.[19] The dissociation of CH_4 over pseudo-T_d WO_4 sites in Na_2WO_4/SiO_2 catalyst is found to be kinetically slower than that on Mn_2O_5 moiety in Mn_2O_5–Na_2WO_4/SiO_2 catalyst, given that the k_d° value for C–H scission in CH_4 over Mn_2O_5 sites is 3 orders of magnitude higher than over the surface Na_2WO_4 sites (Fig. 11). However, the formation of surface intermediates in the case of CH_4 dissociation over

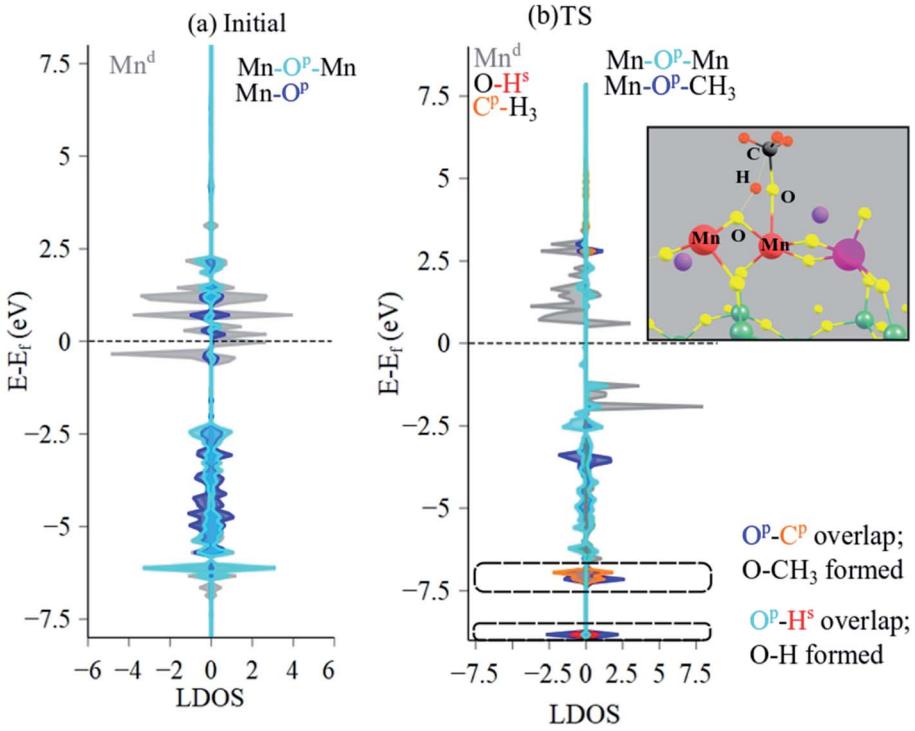

Fig. 10 LDOS analysis of (a) initial, and (b) TS structures, evidencing Mn–O–CH_3 and $(Mn)_2$–O–H formation, suggesting that the CH_4 dissociation is mediated by a TS where a methyl is coordinated to the oxygens on the Mn center, while Mn–O–Mn bridging bond abstracts the hydrogen from the CH_4. E_F value for the initial structure was −2.75 eV and TS was −1.77 eV. Colored atoms correspond to the corresponding color in DOS plots.

Na_2WO_4 surface sites, namely W–CH_3 and W–O–H is endothermic by 0.60 eV. On the other hand, the formation of surface intermediates due to CH_4 dissociation over Mn_2O_5 moiety in Mn_2O_5–Na_2WO_4/SiO_2, namely Mn–O–CH_3 and Mn–O–H, is appreciably exothermic by −0.48 eV. The occupied C 2p states of the CH_3 fragment in Mn–O–CH_3 are more stabilized (*i.e.*, lower in energy) when bound to Mn–O (−7.0 eV) *vs.* when bound to W as in W–CH_3 (−1.7 eV), as shown in Fig. 8 and 10, which explains the enhanced stability of intermediates formed over Mn_2O_5. The higher stability of intermediates formed over Mn_2O_5 moiety increases their likelihood of staying adsorbed and further oxidizing to the unselective CO_x products instead of desorbing as methyl radicals into the gas-phase to form C_2 products.[62] It is known that the selectivity towards C_2 products in OCM relies on the thermodynamics of adsorption of the methyl fragment (ion or radical) on the catalyst, which can lead to further oxidation to CO or CO_2.[63] Therefore, the energy of the adsorbed CH_3 fragment effectively describes the selectivity to C_2 hydrocarbons during the OCM process. Current results can be extrapolated to hypothesize slower kinetics of CH_4 dissociation, but higher C_2 selectivity for CH_4 dissociation over Na_2WO_4 sites in Na_2WO_4/SiO_2 catalysts in comparison to CH_4 dissociation over Mn_2O_5 sites in Mn_2O_5–Na_2WO_4/SiO_2. In agreement with the present hypothesis, experimental results evidence higher CH_4 conversion, but lower C_2 selectivity for Mn–Na_2WO_4/SiO_2 (CH_4 conversion 36%, C_2 selectivity 54%) *vs.* Na_2WO_4/SiO_2 (CH_4 conversion 15%, C_2 selectivity 62%) catalysts in OCM.[64] A recent temporal analysis of products (TAP) reactor study of crystalline phase Mn–Na_2WO_4/SiO_2 catalysts further elucidated that the Na_2WO_4/SiO_2 catalyst (without Mn-oxide) possesses two distinct kinds of oxygen species at 800 °C: (i) a dissolved molecular O_2 type species only released from the molten Na_2WO_4 phase and (ii) an atomic lattice O type species associated with surface Na–WO_4 sites that can be removed by reduction with CH_4.[65] Both these oxygen species are catalytically active for the OCM reaction. On the other hand, the 1.2Mn/SiO_2 catalyst (without

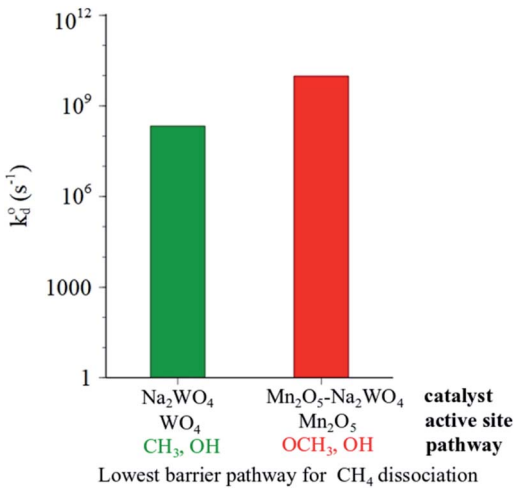

Fig. 11 Comparison of calculated intrinsic rate constants for dominant (lowest barrier) pathways for CH_4 dissociation over the Na_2WO_4/SiO_2 (green) and Mn_2O_5–Na_2WO_4/SiO_2 (red) catalysts.

Na_2WO_4) only provides molecular O_2 type species associated with the Mn-oxide phase, and no atomic O type species. The O_2 species associated with the Mn-oxide phase were found to highly unselective toward C_2 product formation from CH_4 activation.[65] It would be interesting to conduct a similar TAP reactor study on model catalysts in the absence of crystalline oxide phases with only dispersed surface sites present to compare how such dispersed sites function *versus* the respective crystalline oxide phase.

The faster intrinsic kinetics of heterolytic CH_4 dissociation over the Mn_2O_5 sites *versus* the Na_2WO_4 surface sites are not surprising. In fact, DFT calculations have been used to correlate the C–H bond activation energy to the surface reducibility (oxygen vacancy formation energy, work function) in the literature.[63] A linear correlation was found between the C–H activation energy and the oxygen vacancy formation energy of pure/doped metal-oxides, making surface reducibility a descriptor for predicting catalyst activity and selectivity for CH_4 dissociation in OCM.[63] Given that Mn-oxides are more reducible than W-oxides, the CH_4 dissociation over surface Mn_2O_5 sites is expected to be faster than Na_2WO_4. Moreover, according to this correlation between C–H activation barrier and reducibility of the surface metal oxide site, one of the roles of Na-promotion is to increase the reducibility of surface WO_x sites, as evidenced by lowering of peak temperature values during H_2-TPR with Na-addition, reported in a recent study on Na–WO_x/SiO_2 model catalysts.[22]

It is known that MnO_x-based catalysts form excellent partial and total oxidation catalysts owing to their enhanced reducibility. Examples of Mn-oxide based catalysts used for oxidation reactions include: Mn_2O_3 for complete oxidation of methane,[61] Mn-oxide–CeO_2 catalysts for formaldehyde oxidation,[66] Spinel $CoMn_2O_4$ for toluene oxidation,[67] mesoporous Mn-oxide catalysts for water oxidation,[68] alkane oxidation over Mn-perovskites,[69] CeO_2-supported Mn-oxide for propane oxidation,[70] In fact, analogous to the CH_4 dissociation pathway over Mn_2O_5 moiety envisioned in the present study, operando FTIR spectroscopy elsewhere[71] confirmed the formation of Mn–OH surface species by abstraction of hydrogen atoms by nucleophilic oxygen atoms (Mn–O–Mn) from propane during propane oxidation, providing support for the DFT modelling results and chemical insights presented herein.

Recent state-of-the-art understanding regarding the role of Mn- and Na-promoters in Mn_2O_3–Na_2WO_4/SiO_2 OCM catalysts puts chemical insights provided in the present work in perspective. Specifically, it was recently shown *via* experimental CH_4 + O_2 temperature-programmed-surface-reaction of well-defined single site catalysts that Na_2WO_4 surface sites could effectively and selectively activate CH_4 in absence of any Mn-promoter to form C_2 products, making the role of Mn-promoter unclear.[22] Further evidence of the dispersed phase Na–WO_4 surface sites being the critical OCM active sites was provided in recent experimental studies[48,72] where temporal analysis of products (TAP) reactor studies in conjunction with steady-state OCM reaction studies of Na_2WO_4/SiO_2 catalysts (without Mn-oxide) demonstrated that the dispersed surface Na–WO_4 sites were responsible for selectively activating CH_4 to yield C_2 and CO products, while molten Na_2WO_4 phase was found to be mainly responsible for the over-oxidation of CH_4 to CO_2, and oxidative dehydrogenation of C_2H_6 to C_2H_4.[72] Likewise, Mn-containing phases including MnO_x surface oligomers, $MnWO_4$ and Mn–WO_3 nanoparticles in Mn–Na–WO_x/SiO_2 tri-metal oxide model OCM catalyst were found to be primarily spectating during OCM under differential reaction conditions and when such Mn phases are present in small populations.[48] An older model study had previously shown that Na-coordinated WO_4 surface sites were more selective but slightly less active than Mn-coordinated WO_x and uncoordinated WO_x sites during OCM in a series of model bi-metal oxide OCM catalysts.[25] Lastly, *via operando* synchrotron μ-XRF/XRD/absorption-computed tomography, it was shown that crystalline manganese oxide phases including Mn_2O_3, Mn_7SiO_{12} and $MnWO_4$ are not required components to yield an active catalyst,[6] while no conclusion could be reached regarding the dispersed phase Mn_aO_b surface sites that can be present on the SiO_2.[30]

The current study, utilizing *in situ* spectroscopy, *ab initio* molecular dynamics, *ab initio* thermodynamics, and periodic-DFT modelling bridges the knowledge gap present in the literature and provides the following critical mechanistic insights, which suggest that Mn-promotion in fact is likely not essential for a yielding a selective-active OCM catalyst:

(1) CH_4 heterolytically dissociates effectively over the Na_2WO_4 surface sites in absence of Mn-promoter, with a TS barrier of 1.07 eV forming W–CH_3 and W–O–H surface intermediates. The surface intermediate formation is endothermic by 0.60 eV, indicative of their instability and likelihood of facile desorption.

(2) CH_4 heterolytically dissociates over the WO_5 moiety significantly slower when the Mn_2O_5–Na_2WO_4/SiO_2 catalyst is studied due to structural changes incurred upon Mn_2O_5 coordination to the WO_4 site forming the WO_5. This shows that Mn-promotion can infact poison the otherwise pseudo-T_d WO_4 surface active sites, retarding the kinetics of CH_4 dissociation over them.

(3) CH_4 dissociates over the Mn_2O_5 moiety with a TS barrier of 0.72 eV forming Mn–O–CH_3 and $(Mn)_2$–O–H surface intermediates. The surface intermediates formation is appreciably exothermic (−0.48 eV), indicative of the high stability of the formed intermediates.

(4) The significantly higher stability of surface intermediates formed when CH_4 dissociates over the Mn_2O_5 moiety in Mn_2O_5–Na_2WO_4/SiO_2 catalyst *versus* the intermediates formed upon CH_4 dissociation over the Na_2WO_4/SiO_2 signifies the likelihood of the Mn–O–CH_3, $(Mn)_2$–O–H surface intermediates over-oxidizing to CO_x, in agreement with the higher CH_4 conversion but lower C_2 selectivity reported in the OCM literature for MnO_x/SiO_2 catalysts.[64] Therefore, the selective-active sites for OCM are the Na-coordinated WO_4 surface sites present in Na_2WO_4/SiO_2 catalysts without Mn-promotion. Mn promotion can create a second set of Mn-based surface sites (like the surface Mn_2O_5 sites) that are more active for CH_4 dissociation than the WO_4-based sites, but less selective to C_2 products due to the

unfavorable desorption of the reaction intermediates formed over Mn_2O_5.

(5) Computational results herein also suggest that CH_4 activation *via* the MvK mechanism where the oxygen species involved in the reaction originate in the solid phase catalytic active site is quite possible. The DFT-calculated intrinsic barriers of the MvK type reaction pathways are in general agreement with the experimental apparent activation energy values reported in the literature, providing qualitative support for the possibility of the MvK mechanism prevailing during catalytic OCM. However, we note that only the heterolytic CH_4 activation pathway is studied herein and the homolytic CH_4 activation pathway over these surface sites will be addressed in a future study. Literature studies have shown that both heterolytic and homolytic activation of CH_4 occurs during OCM, where both pathways yield CH_3 radicals in the gas-phase.[73,74] Typically, homolytic pathways exhibit higher energy barriers than the heterolytic pathway[55] due to the stabilization of the CH_3 fragment from surface interactions in the heterolytic pathway.

4. Conclusions

The study herein utilized *in situ* spectroscopy, AIMD, AITD, and periodic-DFT to provide unprecedented chemical insights regarding CH_4 activation over Na_2WO_4/SiO_2 *versus* Mn–Na_2WO_4/SiO_2 catalysts. We report, for the first time, that Mn-promotion is not essential to tune the pseudo-T_d WO_4 surface sites known to be active for OCM. Contrary to previous understanding, we show that Mn-promotion poisons the pseudo-T_d Na_2WO_4 surface site, with the resulting surface WO_5 site exhibiting retarded kinetics for CH_4 activation. With Mn-promotion, however, new Mn-based surface sites (Mn_2O_5 in this study) form that can activate CH_4 faster than the WO_4-based surface sites. The surface intermediates formed during CH_4 dissociation over the Mn_2O_5 sites (Mn–O–CH_3, $(Mn)_2$–OH) are more stable than those formed *via* CH_4 dissociation over the Na_2WO_4 site (W–CH_3, W–O–H), and prone to over-oxidation to CO_x due to the unfavorable desorption. Considering these insights that agree with recent state-of-the-art *in situ* and *operando* characterization studies, it is proposed that the addition of MnO_x does not promote the pseudo-T_d, Na-coordinated WO_4 sites where CH_4 activates selectively (*i.e.*, essential selective active sites for OCM). The Mn-promotion likely creates a second set of active MnO_x surface sites that are more active for CH_4 activation, but less C_2 selective than the Na–WO_4 surface sites. These findings contradict Lunsford's OCM model, where the Na–O–Mn sites are hypothesized to be critically involved in the redox mechanism during OCM.[75] The results herein also do not completely agree with Li's OCM model, as W^{6+} is barely seen to reduce during CH_4 dissociation step, while Li proposed that W reduces from +6 to +5/+4 during the CH_4 dissociation step, and Mn_2O_3 provides electron-coupled oxygen-spillover to re-oxidize the reduced W sites back to +6 oxidation state.[76] Lastly, note that the findings herein do not account for the crystalline nanoclusters/nanoparticles (<2–3 nm) of $MnWO_4$ or Mn-contaminated WO_3 which are present in the tri-metal oxide model catalyst studied herein. The exact nature of these nanoclusters/nanoparticles is not understood presently and they can only be modelled accurately to generate structure–function relationships for OCM when their size, shape, surface composition, vacancy/defect density, *etc.* are well-characterized. It suffices to note here that crystalline $MnWO_4$, even when present, does not contribute significantly to OCM.[29,30]

Future investigations on the role of surface MnO_x sites during CH_4 activation in well-defined catalysts should include CH_4 + O_2 temperature-programmed surface reaction, steady state performance tests, isotope-switch experiments in temporal analysis of products (TAP) reactor, and computational analysis of the homolytic pathway for CH_4 activation over the catalyst models generated in this study.

Data availability

Relevant data is present in the ESI file.†

Author contributions

DK and JB conducted all theoretical work. DK and SS conducted spectroscopy experiments. DK, JB, and IEW wrote the manuscript. All authors have agreed to the publication of this manuscript.

Conflicts of interest

The authors declare no competing interests.

Acknowledgements

This work is supported by NSF CBET 1706581. DK also gratefully acknowledges John C. Chen endowed fellowship for financial support. This work used the Extreme Science and Engineering Discovery Environment (XSEDE) (Comet cluster), which is supported by National Science Foundation grant number ACI-1548562, under allocation ID TG-CTS150038 with XSEDE.[77]

References

1 X. Li, J. Xie, H. Rao, C. Wang and J. Tang, *Angew. Chem., Int. Ed.*, 2020, **59**, 19702–19707.
2 A. M. Arinaga, M. C. Ziegelski and T. J. Marks, *Angew. Chem., Int. Ed.*, 2021, **60**, 10502.
3 V. Paunović, G. Zichittella, M. Moser, A. P. Amrute and J. Pérez-Ramírez, *Nat. Chem.*, 2016, **8**, 803–809.
4 M. Moser, L. Rodríguez-García, A. P. Amrute and J. Pérez-Ramírez, *ChemCatChem*, 2013, **5**, 3520–3523.
5 A. Caballero and P. J. Perez, *Chem. Soc. Rev.*, 2013, **42**, 8809–8820.
6 M.-S. Salehi, M. Askarishahi, H. R. Godini, O. Görke and G. Wozny, *Ind. Eng. Chem. Res.*, 2016, **55**, 3287–3299.
7 T. N. Nguyen, T. T. P. Nhat, K. Takimoto, A. Thakur, S. Nishimura, J. Ohyama, I. Miyazato, L. Takahashi, J. Fujima, K. Takahashi and T. Taniike, *ACS Catal.*, 2020, **10**, 921–932.

8 Z. Cheng, D. S. Baser, S. G. Nadgouda, L. Qin, J. A. Fan and L.-S. Fan, *ACS Energy Lett.*, 2018, **3**, 1730–1736.
9 S. Parishan, P. Littlewood, A. Arinchtein, V. Fleischer and R. Schomäcker, *Catal. Today*, 2018, **311**, 40–47.
10 A. L. Tonkovich, R. W. Carr and R. Aris, *Science*, 1993, **262**, 221.
11 X. Guo, G. Fang, G. Li, H. Ma, H. Fan, L. Yu, C. Ma, X. Wu, D. Deng, M. Wei, D. Tan, R. Si, S. Zhang, J. Li, L. Sun, Z. Tang, X. Pan and X. Bao, *Science*, 2014, **344**, 616–619.
12 K. Takahashi, L. Takahashi, T. N. Nguyen, A. Thakur and T. Taniike, *J. Phys. Chem. Lett.*, 2020, **11**, 6819–6826.
13 L. Grajciar, C. J. Heard, A. A. Bondarenko, M. V. Polynski, J. Meeprasert, E. A. Pidko and P. Nachtigall, *Chem. Soc. Rev.*, 2018, **47**, 8307–8348.
14 P. Schlexer Lamoureux, K. T. Winther, J. A. Garrido Torres, V. Streibel, M. Zhao, M. Bajdich, F. Abild-Pedersen and T. Bligaard, *ChemCatChem*, 2019, **11**, 3581–3601.
15 J. A. Labinger, *Science*, 1995, **269**, 1833.
16 D. Kiani, S. Sourav, Y. Tang, J. Baltrusaitis and I. E. Wachs, *Chem. Soc. Rev.*, 2021, **50**, 1251–1268.
17 D. Kiani, G. Belletti, P. Quaino, F. Tielens and J. Baltrusaitis, *J. Phys. Chem. C*, 2018, **122**, 24190–24201.
18 R. K. Grasselli and A. W. Sleight, in *Studies in Surface Science and Catalysis*, ed. R. K. Grasselli and A. W. Sleight, Elsevier, 1991, vol. 67, p. ix.
19 D. Kiani, S. Sourav, J. Baltrusaitis and I. E. Wachs, *ACS Catal.*, 2019, **9**, 5912–5928.
20 Z. Li, S. Ji, Y. Liu, X. Cao, S. Tian, Y. Chen, Z. Niu and Y. Li, *Chem. Rev.*, 2020, **120**, 623–682.
21 L. Zhang, M. Zhou, A. Wang and T. Zhang, *Chem. Rev.*, 2020, **120**, 683–733.
22 D. Kiani, S. Sourav, I. E. Wachs and J. Baltrusaitis, *Catal. Sci. Technol.*, 2020, **10**, 3334–3345.
23 I. E. Wachs and K. Routray, *ACS Catal.*, 2012, **2**, 1235–1246.
24 S. Arndt, T. Otremba, U. Simon, M. Yildiz, H. Schubert and R. Schomäcker, *Appl. Catal., A*, 2012, **425–426**, 53–61.
25 D. Kiani, S. Sourav, W. Taifan, M. Calatayud, F. Tielens, I. E. Wachs, J. Baltrusaitis, I. E. Wachs and J. Baltrusaitis, *ACS Catal.*, 2020, **10**, 4580–4592.
26 W. Riedel, L. Thum, J. Möser, V. Fleischer, U. Simon, K. Siemensmeyer, A. Schnegg, R. Schomäcker, T. Risse and K.-P. Dinse, *J. Phys. Chem. C*, 2018, **122**, 22605–22614.
27 W. Pengwei, Z. Guofeng, Y. Wang, L. Yong, P. Wang, G. Zhao, Y. Wang and Y. Lu, *Sci. Adv.*, 2017, **3**, 1–10.
28 P. Wang, G. Zhao, Y. Liu and Y. Lu, *Appl. Catal., A*, 2017, **544**, 77–83.
29 M. J. Werny, Y. Wang, F. Girgsdies, R. Schlögl and A. Trunschke, *Angew. Chem., Int. Ed.*, 2020, **59**, 14921.
30 A. Vamvakeros, D. Matras, S. D. M. Jacques, M. di Michiel, S. W. T. Price, P. Senecal, M. A. Aran, V. Middelkoop, G. B. G. Stenning, J. F. W. Mosselmans, I. Z. Ismagilov and A. M. Beale, *J. Catal.*, 2020, **386**, 39–52.
31 H. Guesmi, R. Grybos, J. Handzlik and F. Tielens, *RSC Adv.*, 2016, **6**, 39424–39432.
32 K. Kurleto, F. Tielens and J. Handzlik, *J. Phys. Chem. C*, 2020, **124**(5), 3002–3013.
33 M. Lahti, A. Chaudhuri, K. Pussi, D. Hesp, I. M. McLeod, V. R. Dhanak, M. O. King, M. Kadodwala and D. A. MacLaren, *Surf. Sci.*, 2014, **622**, 35–43.
34 http://www.p4vasp.at/, 2021.
35 M. Yu and D. R. Trinkle, *J. Chem. Phys.*, 2011, **134**, 064111.
36 G. Henkelman, B. P. Uberuaga and H. Jónsson, *J. Chem. Phys.*, 2000, **113**, 9901–9904.
37 G. Henkelman and H. Jónsson, *J. Chem. Phys.*, 2000, **113**, 9978–9985.
38 G. Li, P. Vassilev, M. Sanchez-Sanchez, J. A. Lercher, E. J. M. Hensen and E. A. Pidko, *J. Catal.*, 2016, **338**, 305–312.
39 N. Kosinov, A. S. G. Wijpkema, E. Uslamin, R. Rohling, F. J. A. G. Coumans, B. Mezari, A. Parastaev, A. S. Poryvaev, M. V. Fedin, E. A. Pidko and E. J. M. Hensen, *Angew. Chem.*, 2018, **130**, 1028–1032.
40 G. Li, I. Vollmer, C. Liu, J. Gascon and E. A. Pidko, *ACS Catal.*, 2019, **9**, 8731–8737.
41 *The Materials Project, Materials Data on Mn2O3 by Materials Project*, United States, 2014, DOI: 10.17188/1272415.
42 Y.-B. Kang and I.-H. Jung, *Metall. Mater. Trans. E*, 2016, **3**, 156–170.
43 W. E. W. E. Taifan, T. Bučko and J. Baltrusaitis, *J. Catal.*, 2017, **346**, 78–91.
44 M. W. Chase Jr, *NIST-JANAF thermochemical tables*, American Chemical Society, American Institute of Physics for the National Institute of Standards and Technology, Washington, DC, New York, 4th edn, 1998.
45 K. K. Irikura, *J. Phys. Chem. Ref. Data*, 2007, **36**, 389–397.
46 K. Reuter and M. Scheffler, *Phys. Rev. B*, 2001, **65**, 035406.
47 R. Jutta and K. Reuter, *Max-Planck-Gesellschaft Zur Foerderung Der Wissenschaften ev Berlin (GERMANY FR)*, Fritz-Haber-INST, 2006.
48 D. Kiani, S. Sourav, J. Baltrusaitis and I. E. Wachs, *ACS Catal.*, 2021, **11**, 10131–10137.
49 F. Yang, J. Graciani, J. Evans, P. Liu, J. Hrbek, J. F. Sanz and J. A. Rodriguez, *J. Am. Chem. Soc.*, 2011, **133**, 3444–3451.
50 E. I. Ross-medgaarden and I. E. Wachs, *J. Phys. Chem. C*, 2007, **111**, 15089–15099.
51 S. Lwin, Y. Li, A. I. Frenkel and I. E. Wachs, *ACS Catal.*, 2016, **6**, 3061–3071.
52 Q. Wan, V. Fung, S. Lin, Z. Wu and D.-e. Jiang, *J. Mater. Chem. A*, 2020, **8**, 4362–4368.
53 K. Takanabe and E. Iglesia, *J. Phys. Chem. C*, 2009, **113**, 10131–10145.
54 Z. Liu, J. P. Ho Li, E. Vovk, Y. Zhu, S. Li, S. Wang, A. P. van Bavel and Y. Yang, *ACS Catal.*, 2018, **8**, 11761–11772.
55 M. C. Cholewinski, M. Dixit and G. Mpourmpakis, *ACS Omega*, 2018, **3**, 18242–18250.
56 J. Wu, S. Li, J. Niu and X. Fang, *Appl. Catal., A*, 1995, **124**, 9–18.
57 S.-f. Ji, T.-c. Xiao, S. S.-B. B. Li, C.-z. Xu, R.-l. Hou, K. S. Coleman, M. L. H. Green, J. Wu, S. S.-B. B. Li, Z. C. Jiang, C. J. Yu, X. P. Fang, S. S.-B. B. Li, H. L. Wang, J. Wu, S. S.-B. B. Li, J. Niu, X. P. Fang, D. J. Wang, M. P. Rosynek, J. H. Lunsford, S. S.-B. B. Li, A. Palermo, J. Pedro, H. Vazquez and R. M. Lambert, *Appl. Catal., A*, 1995, **68**, 191–196.

58 J. Wu and S. Li, *J. Phys. Chem.*, 1995, **99**, 4566–4568.
59 S. Ji, T. Xiao, S. Li, L. Chou, B. Zhang, C. Xu, R. Hou, A. P. E. E. York and M. L. H. H. Green, *J. Catal.*, 2003, **220**, 47–56.
60 S. Li, *J. Nat. Gas Chem.*, 2003, **12**, 1–9.
61 Y.-F. Han, K. Ramesh, L. Chen, E. Widjaja, S. Chilukoti and F. Chen, *J. Phys. Chem. C*, 2007, **111**, 2830–2833.
62 M. J. Capitan, J. A. Odriozola, A. Marquez and J. F. Sanz, *J. Catal.*, 1995, **156**, 273–278.
63 G. Kumar, S. L. J. Lau, M. D. Krcha and M. J. Janik, *ACS Catal.*, 2016, **6**, 1812–1821.
64 S. Hou, Y. Cao, W. Xiong, H. Liu and Y. Kou, *Ind. Eng. Chem. Res.*, 2006, **45**, 7077–7083.
65 S. Sourav, Y. Wang, D. Kiani, J. Baltrusaitis, R. R. Fushimi and I. E. Wachs, *ACS Catal.*, 2021, **11**, 10288–10293.
66 J. Quiroz, J.-M. Giraudon, A. Gervasini, C. Dujardin, C. Lancelot, M. Trentesaux and J.-F. Lamonier, *ACS Catal.*, 2015, **5**, 2260–2269.
67 C. Dong, Z. Qu, Y. Qin, Q. Fu, H. Sun and X. Duan, *ACS Catal.*, 2019, **9**, 6698–6710.
68 C.-H. Kuo, I. M. Mosa, A. S. Poyraz, S. Biswas, A. M. El-Sawy, W. Song, Z. Luo, S.-Y. Chen, J. F. Rusling, J. He and S. L. Suib, *ACS Catal.*, 2015, **5**, 1693–1699.
69 G. Koch, M. Hävecker, D. Teschner, S. J. Carey, Y. Wang, P. Kube, W. Hetaba, T. Lunkenbein, G. Auffermann, O. Timpe, F. Rosowski, R. Schlögl and A. Trunschke, *ACS Catal.*, 2020, **10**, 7007–7020.
70 H. Wang, H. Zhou, S. Li, X. Ge, L. Wang, Z. Jin, C. Wang, J. Ma, X. Chu, X. Meng, W. Zhang and F.-S. Xiao, *ACS Catal.*, 2020, **10**, 10559–10569.
71 X. Li, D. Teschner, V. Streibel, T. Lunkenbein, L. Masliuk, T. Fu, Y. Wang, T. Jones, F. Seitz, F. Girgsdies, F. Rosowski, R. Schlögl and A. Trunschke, *Chem. Sci.*, 2019, **10**, 2429–2443.
72 S. Sourav, Y. Wang, D. Kiani, J. Baltrusaitis, R. R. Fushimi and I. E. Wachs, *Angew. Chem., Int. Ed.*, 2021, **60**, 21502.
73 J. H. Lunsford, *Angew. Chem., Int. Ed. Engl.*, 1995, **34**, 970–980.
74 D. Dissanayake, J. H. Lunsford and M. P. Rosynek, *J. Catal.*, 1994, **146**, 613–615.
75 D. J. Wang, M. P. Rosynek and J. H. Lunsford, *J. Catal.*, 1995, **155**, 390–402.
76 S. Li, *J. Nat. Gas Chem.*, 2003, **12**, 1–9.
77 J. Towns, T. Cockerill, M. Dahan, I. Foster, K. Gaither, A. Grimshaw, V. Hazlewood, S. Lathrop, D. Lifka, G. D. Peterson, R. Roskies, J. R. Scott and N. Wilkins-Diehr, *Comput. Sci. Eng.*, 2014, **16**, 62–74.